Fast evaluation of Photomask Near-Fields in Sub-Wavelength 193nm Lithography

Jaione Tirapu-Azpiroz and Eli Yablonovitch

Electrical Engineering Department, UCLA
Los Angeles 90095-1594
jaione@ee.ucla.edu.edu, eliy@ee.ucla.edu
phone: 1 310 206 3724, 1 310 206 2204

ABSTRACT

Sub-wavelength lithography places a serious limitation on the conventional "thin mask" approximation of the field immediately behind the patterned mask. This approximation fails to account for the increasingly important topographical effects of the mask or "thick mask" effects. This approximation of the photomask near-fields results from the direct application of Kirchhoff Boundary Conditions, which multiply the incident field by a binary transmission function of the patterned mask. Polarization dependent edge diffraction effects, as well as phase and amplitude transmission errors that arise from the vector nature of light, and the finite thickness of the substrate and chrome layers, produce significant errors in the scalar simulations of the lithographic image.

Based on the comparison of aerial images at the wafer plane produced by both rigorous electromagnetic solutions of the field on the mask and their "thin mask" counterparts, a more accurate model is proposed that consists of a fixed-width, locally-determined boundary layer of imaginary transmission coefficient added to every edge of the initial "thin mask" approximation. The accuracy of the resultant Boundary Layer model has been exhaustively tested against rigorously simulated aerial images of isolated as well as periodic features of very different profiles and dimensions. The conclusion being that this simple approach is capable of modeling "thick mask" effects at both 248nm and 193nm wavelength and high NA lithography. This greatly improves the accuracy of aerial image computation in photolithography simulations at a reasonable computational cost.

Keywords: Thin mask model, Thick mask, Phase-shifting Masks, Aerial image simulation, Kirchhoff Boundary Conditions, Deep Ultraviolet Lithography, Photomask Near-Field

1. INTRODUCTION

Direct application of Kirchhoff's Boundary Conditions[1] provides a thin mask approximation of the object field on the exit surface of the mask as illustrated in figure 1(a), obtained by multiplying the incident field times an ideal transmission function with the mask pattern. This model ignores diffraction and polarization effects present in the rigorous aperture field of figure 1(b). Although providing reasonably accurate results with mask features larger than the wavelength, it turns out to be very inaccurate for feature sizes of the order of the wavelength[2].

The utilization of 193nm wavelength lithography with a 0.85 NA to print 65nm wafer features translates into a k_1 factor approaching values around 0.3 and mask features of the order of the wavelength for $4X$ magnification. In addition, Alternating Phase-Shifting Masks (Alt. PSM) employ etching profiles with abrupt discontinuities and trench depths also in the order of the wavelength for 180° phase-shifting openings. As a consequence of wavelength sized and high aspect ratio mask features, mask topography effects are becoming an increasing source of simulation errors[3], which are particularly critical for Alternating Phase-Shifting masks[4], and demand rigorous resource-consuming 3D electromagnetic field simulations in the subwavelength regime.

Alternative modeling methods have therefore been studied in literature[5–7]. Lam and Neureuther's recent "Domain Decomposition Method"[7] employs pre-calculated diffracted fields from isolated edges that are added afterwards according to the diffracting patterns. Yan's approach[6] shares with our boundary layer model the
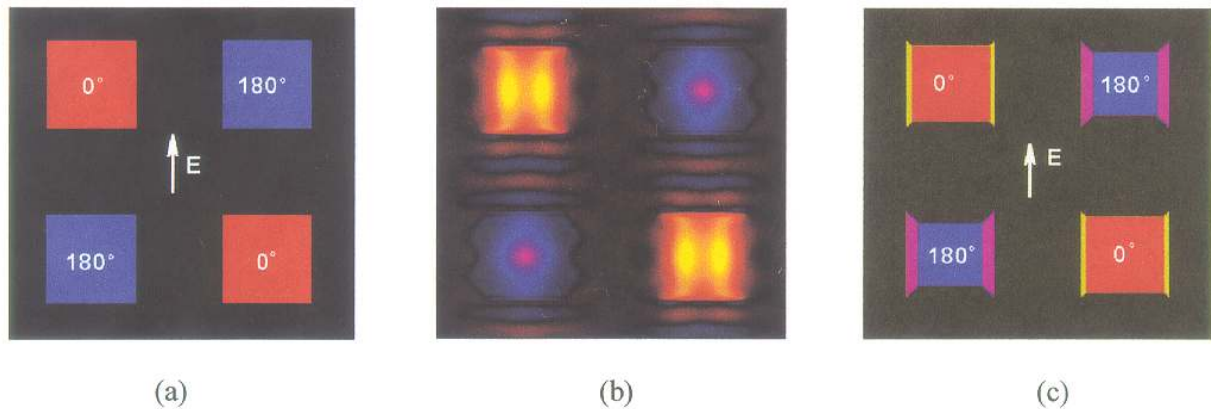
Figure 1. (a) Kirchhoff scalar approximation (thin mask model) of the field on the mask plane of a 2λ half-pitch array of alternating 180°-shifter and clear square mask openings, with vertically polarized electric field. (b) Sketch of the actual object field obtained by rigorous electromagnetic FDTD Tempest simulation on the same mask. (c) Boundary Layer model for the same mask features and illumination conditions.

possibility of locally modeling topographical mask effects with a boundary band of different transmission coefficient at the thin mask edges. Yan's approximates the diffraction effects on the edges of Extreme Ultraviolet Lithography (EUVL) infinite lines of width 2.23λ, by adding a strip to the thin mask model. However in his approach, the width and transmission coefficients of the boundary layer were obtained by matching the diffraction ripples of the near field evaluated on the mask surface. For the complex DUVL transmission masks analyzed in this paper, we performed a systematic study of rectangles of different aspect ratios and sizes, and selected the boundary layer parameters to optimize the fidelity of the central field amplitude on the wafer, not the mask.

2. BOUNDARY LAYER MODEL

The justification for our Boundary Layer Model is as follows. Aerial images at the wafer plane produced by rigorous em solutions of the field on the mask were evaluated by means of a vectorial formulation of the imaging process, and compared to those due to thin mask approximations where the field on the mask openings was replaced by the incident field. We observed that the relative errors of the real and imaginary field components on the wafer follow an inverse law on the opening mean size and height, respectively.

For both square and rectangular openings illuminated by a coherent, normally incident, plane wave, the deficit on the real part of the field main polarization component follows a reciprocal dependence on the size of the opening measured as the harmonic mean of its width (w) and its height (h). (The harmonic mean is defined as twice the product of the sides divided by its sum). As outlined in equation (1), this inverse dependence of the relative amplitude error on the opening size indicates that the error can be assumed proportional to a correction width, Δd, uniform with the size of the opening and to be applied on all four sides of the thin mask model regardless of polarization.

$$Amplitude \; deficit = \frac{\Delta \mathbf{E}}{\mathbf{E}} = \frac{4\Delta d}{d} = \frac{4\Delta d}{\frac{2wh}{w+h}} = \frac{(2w+2h)\Delta d}{wh} = \frac{Boundary \; Layer \; Area}{Total \; Area} \; . \qquad (1)$$

We found that the same inverse law holds for the imaginary part of the aerial field relative to the thin mask field, versus the opening height, dimension defined as the side length in the direction perpendicular to the electric field polarization as formulated in equation (2). Consequently, the Boundary Layer has a purely imaginary transmission coefficient, $-j\beta$, that is proportional to the absolute value of the cosine angle between the electric field polarization and the edge direction, reaching its maximum value when the electric field is

tangent to the boundary, and diminishing to zero when the field is normal to it. This simple geometric rule (cosine rule) accounts for the orientation dependence of the boundary conditions at the metal edges.

$$Relative\,Imaginary\,Error = \frac{Im\{\Delta\mathbf{E}\}}{\mathbf{E}} = \beta\frac{2\Delta d}{h}. \tag{2}$$

The key result of our simulations is that the thick mask effects can be interpreted, to a good approximation, as an intrinsic edge property, and modeled with just two fixed parameters: width and transmission coefficient of a locally-applied boundary layer. Usually, the width of the boundary layer controls the variation in peak amplitude, while the imaginary transmission coefficient corrects phase deviations of the thick mask. These errors differ for different types of mask edge cross-sections, giving different boundary layer parameters to be applied locally in the vicinity of each type of mask edge profile.

Data was collected to determine the boundary layer parameters of three types of etching profiles commonly used in Alt. PSM and illustrated in figure 2: clear and 180° phase-shift opening with and without 35 nm undercut, for two imaging configurations: a $4X$ projection system with NA= 0.68, operating at $\lambda = 248nm$ (Case I of Table 1); and a similar $4X$ system with $NA = 0.85$, and $\lambda = 193nm$ (Case II of Table 1). The procedure for obtaining the optimized values of Boundary Layer width and transmission coefficients was thoroughly explained for the 248nm and 0.68 NA lithography case in a previous publication[8] . There was further shown a remarkable reduction of the error caused by the conventional Kirchhoff approximation, even for mask features close to the wavelength, when the boundary layer is incorporated in the way illustrated in figure 1(c).

Table 1.
Width and transmission coefficients of the boundary layer model for different type of openings in typical Alt. PSM geometry (cases I and II refer to 248nm and 193nm wavelength imaging systems, respectively)

Opening type	Boundary Width(nm)		Tangential Boundary Transmission		Normal Boundary Transmission	Interior Transmission	Minimun opening(nm)	
	I	II	I	II			I	II
Clear	24.8	14.5	0.0i	0.8i	0	1	248	200
Shifter	55.8	53.0	-0.52i	-0.30i	0	-1	300	250
Shifter with 35nm undercut	37.2	33.7	-0.66i	-0.635i	0	-1	350	200

Scalar diffraction theory[1] yields accurate results of the field in the image space when numerical apertures up to 0.7 are employed[9, 10] , but it fails to account for the polarization and oblique direction of propagation of the vector components of the em field with higher NA. In this paper, the 193nm 0.85 NA lithography case is analyzed by means of a vectorial formulation of the imaging process[11] consistent with techniques based on
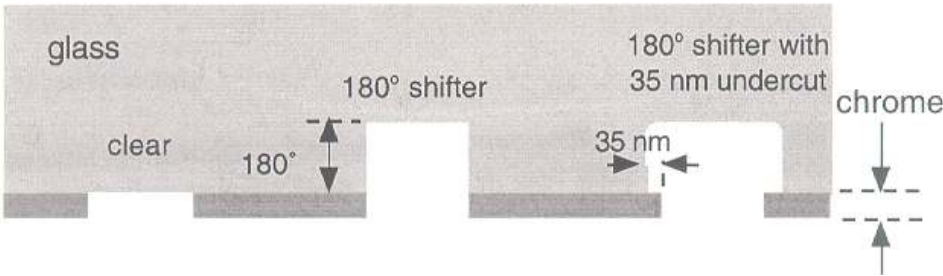

Figure 2. Cross section of the three types of openings considered in this paper for a transmission Alt. Phase-shifting masks.

Huygens-Fresnel principle[12] or plane-wave decomposition[13]. The boundary layer model was optimized for the field component along the direction of polarization of the incident light (E_x component), however it provided similar error reductions for all cross-field components arising at the exit pupil of a high NA lens. This can be observed in figures 3(a) and (b), where the intensity and the phase of the aerial field components at the plane of the wafer for both the conventional thin mask model (dashed line) and the boundary layer model (dashed-dot line) are compared to the actual image (solid line) of a 1.6λ square mask opening. Electromagnetic coupling onto the cross-polarized component (E_y component) was negligible relative to the contribution of the component along the optical axis (E_z component), and it is not considered in fig. 3. The Boundary Layer accurately models the rigorous aerial image amplitude and phase, achieving a remarkable reduction of the errors due to the "thin mask" approximation in both E_x and E_z field components. Moreover, the Boundary Layer model provides accurate results for all the range of feature types and dimensions analyzed in this paper as indicated by the root mean squared error (rms) on the field intensity integrated over the wafer plane area, plotted on figures 4(a)-(c).

3. SIMULATIONS

Systematic simulations of rectangular openings with side sizes ranging from 1λ to 6λ, aspect ratios ranging from 3:1 to 1:3, and three different etching profiles per opening size: 0°, 180° shifter and 180° shifter with 35 nm undercut, provide a means to analyze thick mask effects[8]. 3D Tempest[14] simulations with coherent, on-axis and off-axis illumination provided rigorous electromagnetic results for the fields on the masks. A full vectorial formulation of the imaging process[11] was applied to the evaluation of the aerial field distributions. Two sets of illumination parameters were evaluated: a $4X$ projection system with NA equal to 0.68, operating at 248nm illumination wavelength corresponding to case I of Table 1; and a similar $4X$ system with 0.85 NA, operating at 193nm corresponding to case II in Table 1. The indices of refraction of the glass and chrome are
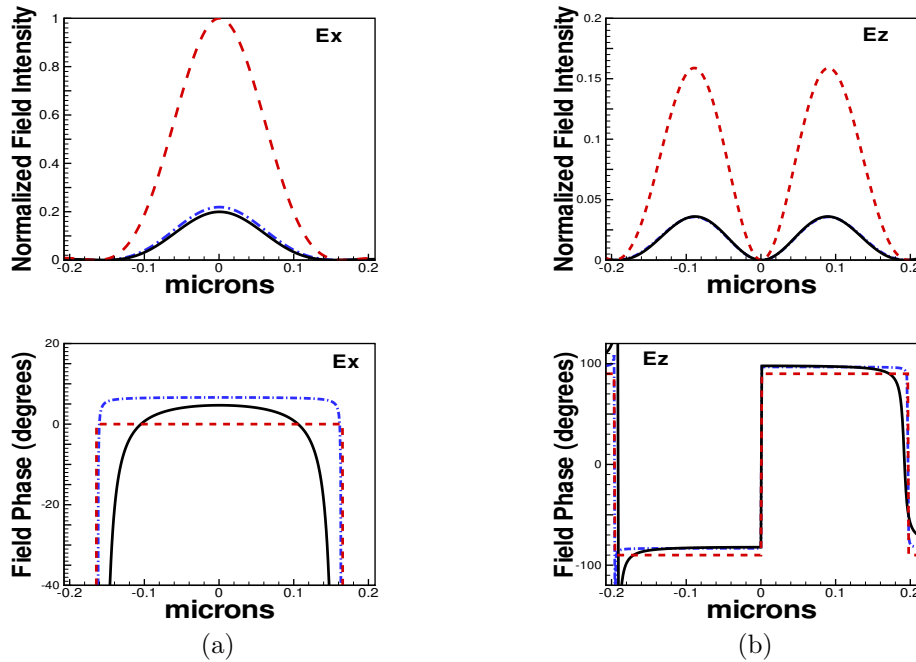
Figure 3. Comparison between the aerial field components produced by rigorously evaluated EM Tempest field solutions of the object field (solid) and both the corresponding "thin mask" approximation (dashed) and our Boundary Layer model (dash-dotted), of a 1.6λ 180°-phase-shift square mask opening. (a) Intensity and phase of the field component along the polarization direction (x-axis) and (b) intensity and phase of the field coupled onto the component along the optical axis (z-axis).

1.5 and 2.5-i2, respectively, at 248nm, and 1.563 and 0.84-i1.65 at 193nm. Finally, a chrome layer thickness of 95nm was employed at 193nm wavelength such that it provided the same absorption of incident light as the 80 nm chrome layer used at 248nm wavelength.

Partial coherence illumination was simulated by assuming Kohler's configuration in which an incoherent light source is located on the focal plane of the condenser lens. The extended source is spatially divided into a number of mutually incoherent point sources, each of them originates a plane wave emerging from the condenser with an angle determined by the source point location with respect to the optical axis. We treated the illumination due to each source point as coherent, polarized plane waves with different angles of incidence, that in practice requires separate results for both orthogonal (TE and TM) polarizations to be incoherently superposed. The aerial image is then obtained by an incoherent superposition of all the contributions. This procedure, known as Abbe's method, yields the image field amplitude and phase distribution for each illumination angle prior to the source integration, needed to determine our boundary layer model. The equivalent Hopkins method used in much of the lithography provides only intensity, and is not as useful for determining boundary layer phase shifts.
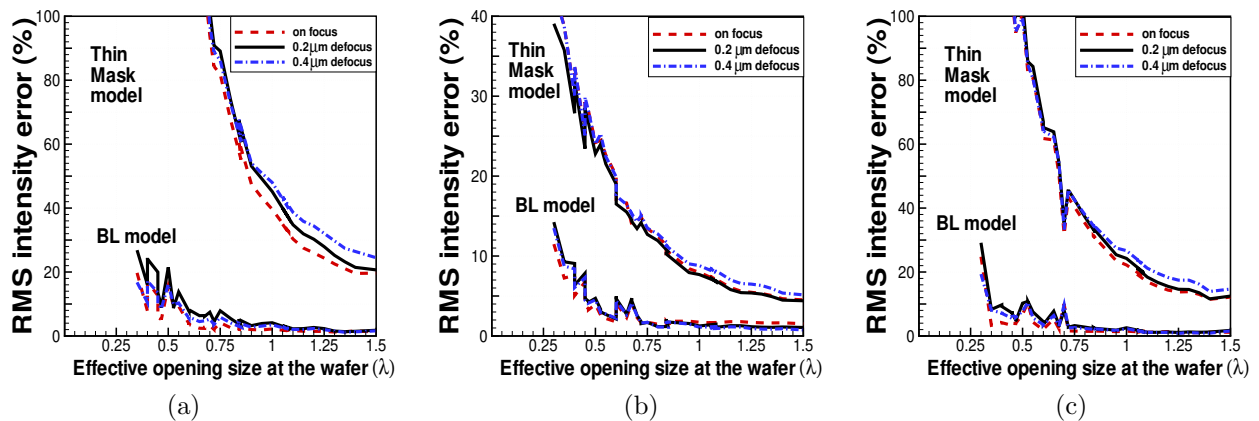
4. RESULTS

Figure 5 is a plot of the root mean squared (rms) error in the intensity distribution integrated over the wafer plane, of the approximated images relative to the rigorous em fields. Unpolarized (both TE and TM components were added incoherently), partially coherent illumination was used at 193nm, $NA = 0.85$ and σ=0.6. A $4X$ reduction ratio was assumed in the simulations, such that even with high $NA = 0.7 - 0.9$, the angle described by the waves collected at the entrance pupil is small, and the same boundary layer parameters of Table 1, optimized for on-axis illumination, can be applied to approximate the near field effects of all off-axis source contributions. Phase errors, which are more critical when the image is out of focus, need to be appropriately compensated by the Boundary Layer model of the object field. In order to evaluate phase effects on the model, three focus planes are analyzed in figure 5, showing that the effect of defocusing (depth-of-field) on the Boundary Layer model is small.

It was further observed that large errors occurred for mask openings with side sizes equal to 1λ, which hardly transmit any electromagnetic field, and were omitted in figures 4 and 5. Current computational approximations are unable to model such small mask openings, and it is recommended that they should be forbidden in the design rules. The minimum recommended opening is 1.2λ.

Finally, we also included an analysis of the accuracy of the Boundary Layer model when applied to periodic mask patterns such as those of figure 1, which generated the images of figure 6. Figure 1(a) represents
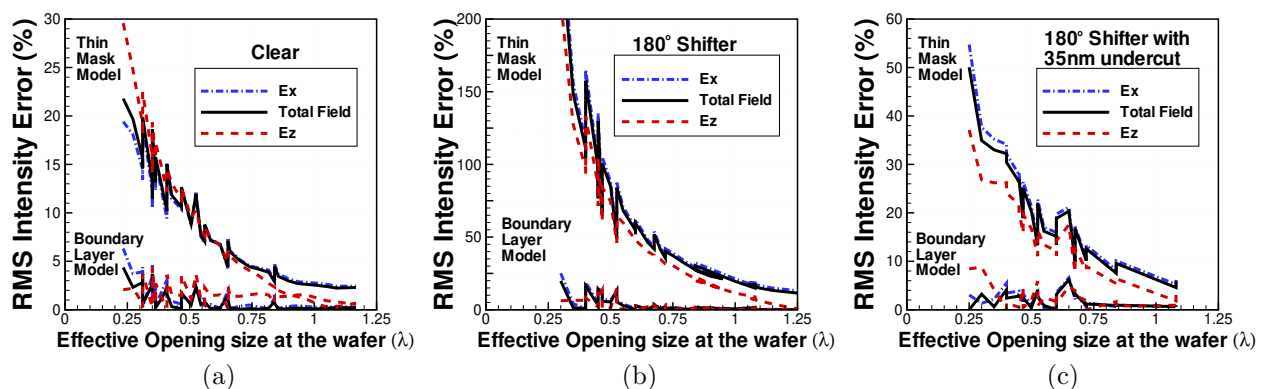
Figure 4. Root mean squared error on the projected image intensity integrated over the wafer plane for the total field and both the E_x and E_z components by a 193nm with 0.85 NA system and coherent illumination.

Figure 5. Root mean squared error in the intensity distribution, integrated over the focal plane and at two out-of-focus positions, of the approximated images relative to the rigorous em fields for unpolarized, partially coherent illumination at 193nm, $NA = 0.85$, $\sigma = 0.6$. Three model parameters are analyzed: (a) 180°-phase-shift openings, (b) clear openings and (c) 180°-phase-shift with 35nm undercut openings.
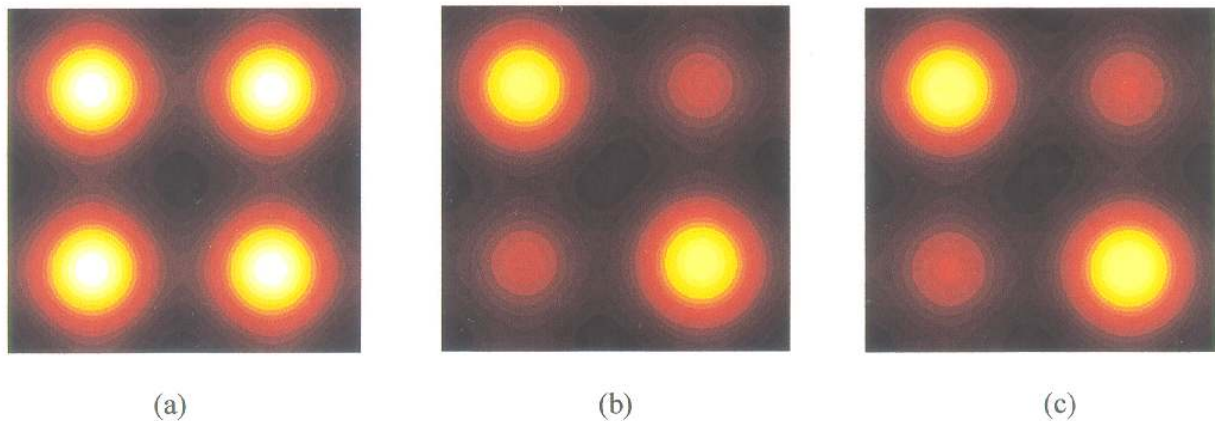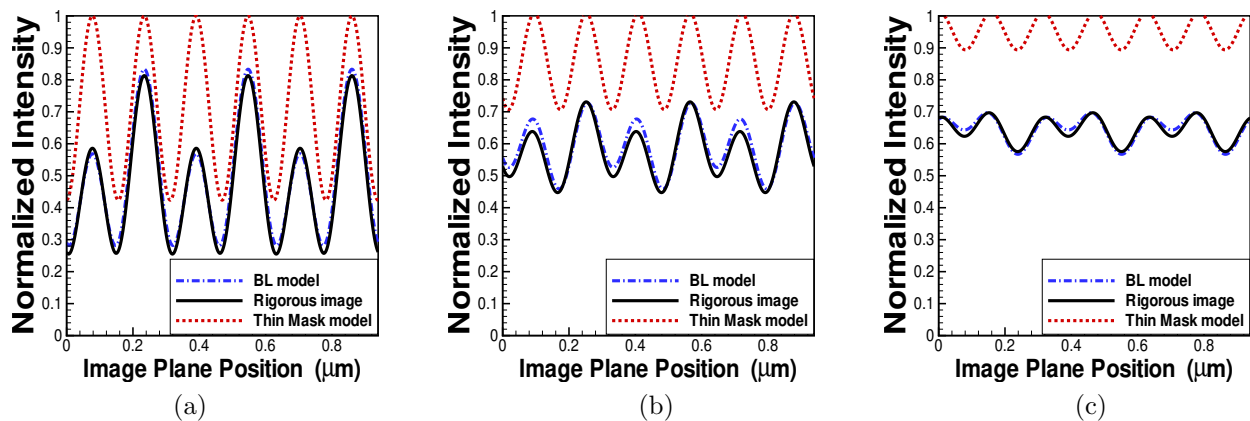

Figure 6. (a) Aerial image intensity distribution at the focal plane obtained from the thin mask approximation of a 2λ half-pitch array of alternating 180°-shifter and clear square mask openings, and producing a rms error of 85.15%. Unpolarized (TE and TM components were added incoherently), $\sigma = 0.6$ partially coherent illumination at 193nm and $NA = 0.85$ was used. (b) Aerial intensity distribution for the rigorously evaluated object field, and (c) aerial intensity distribution obtained with the Boundary Layer model under identical illumination conditions and producing a rms error of 3.48%.

the Kirchhoff scalar approximation (thin mask model) of a 2λ half-pitch array of alternating 180°-shifter and clear square mask openings, with vertically polarized electric field. Figure 1(b) shows a sketch of the actual object field obtained by rigorous electromagnetic FDTD Tempest simulation on the mask plane of the same mask pattern and, figure 1(c) shows the Boundary Layer model for the same mask features and illumination conditions. Figures 6(a)-(c) correspond to the aerial image intensity at the focal plane for the rigorously evaluated object field and its two types of approximations. Unpolarized, $\sigma = 0.6$ partially coherent illumination at 193nm was used with a $NA = 0.85$ imaging system. Figures 6(b), produced by the rigorously evaluated object field, and 6(c), corresponding to the Boundary Layer model, show a close agreement with only a 3.48% rms error due to the approximation. However, Figure 6(a), obtained from the Thin Mask approximation, produced a much higher rms error of 85.15% as compared to the actual image.
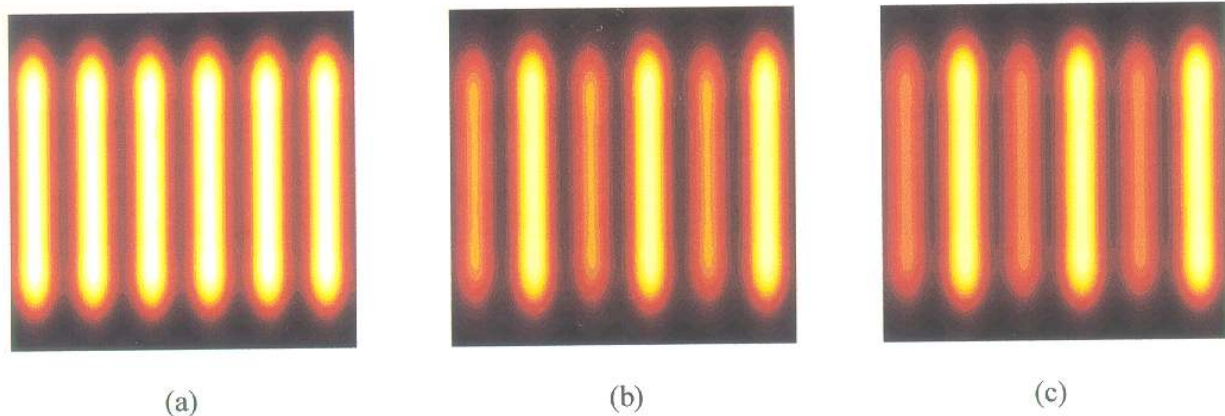
Figure 7. Aerial image intensity results at the focal plane of a 78nm (as measured at the wafer plane) half-pitch array of alternating 180°-shifter and clear rectangular openings with an unpolarized, $\sigma = 0.5$ partially coherent illumination at 193nm and $NA = 0.85$. (a) Aerial image produced by the thin mask approximation with an rms error of 50.97%. (b) Aerial image produced by the rigorously evaluated object field, and (c) aerial image produced by the Boundary Layer with an rms error of 4.63%.

Figure 8. Cross section of the aerial image intensity distribution of a 78nm (as measured at the wafer plane) half-pitch array of alternating 180°-shifter and clear rectangular openings. Unpolarized, $\sigma = 0.5$ partially coherent illumination at 193nm and $NA = 0.85$ was used. (a) Image at the focus plane, (b) effect of defocus at $0.2\mu m$ out-of-focus and (c) at $0.4\mu m$ out-of-focus.

Similarly, figures 7(a)-(c) represent the aerial images generated by the Thin Mask approximation, the rigorously evaluated object field and the Boundary Layer model, respectively, of a 78nm (as measured at the wafer plane) half-pitch array of alternating 180°-shifter with clear rectangular features. Unpolarized, $\sigma = 0.5$ partially coherent illumination at 193nm was used with a $NA = 0.85$ imaging system. The Boundary Layer model produced a rms error of 4.63% while the rms error due to the Thin Mask approximation was of 50.67% as compared to the rigorous image. A cross-section of the three aerial images at the focal plane is plotted on figure 8(a) and at $0.2\mu m$ and 0.4 μm defocus on figures 8(b) and (c), respectively. It can be observed how the Boundary Layer model yields accurate field approximations within the depth-of-focus of the optical projection system.

5. CONCLUSIONS

Next generation Alternating Phase-Shifting masks have etching profiles with abrupt discontinuities, mask features of the order of the wavelength and high aspect ratios. Rigorously evaluated fields on thick chrome mask apertures exhibit diffraction and polarization effects (Thick Mask effects) that can not be accurately modeled by the conventional Thin Mask approximation.

The key result of our simulations is that the thick mask effects can be interpreted, to a good approximation, as an intrinsic edge property, and modeled with just two fixed parameters: width and transmission coefficient of a locally-determined boundary layer. Thus our proposed model consists of a sophisticated version of Kirchhoff approximation, simply adding a boundary layer to every edge. We proved in this paper that the BL model accurately accounts for thick mask effects of the fields on the mask, incorporating effects of electromagnetic coupling due to the high numerical aperture ≥ 0.7, and accurately compensates for phase errors even at planes out of focus. This greatly improves the accuracy of aerial image computation in photolithography simulations at a reasonable computational cost.

ACKNOWLEDGMENTS

REFERENCES

1. M. Born and E. Wolf, *Principles of Optics*, Pergamon Press, 6th ed., 1987.
2. M. S. Yeung and E. Barouch, "Limitation of the kirchhoff boundary conditions for aerial image simulation in 157 nm optical lithography," *IEEE Electron Device Lett.* **21 No 9**, pp. 433–435, Sep. 2000.
3. C. Pierrat and A.Wong, "The mef revisited: Low k_1 effects versus mask topography effects," *Proceedings of the SPIE* **5040**, pp. 193–202, 2003.
4. Y. Borodovsky and et. al., "Lithography strategy for 65nm node," *Proceedings of the SPIE* **4346**, 2002.
5. K. Adam and A. R. Neureuther, "Simplified models for edge transitions in rigorous mask modeling," *Proc. of the SPIE* **4346 pt.1-2**, pp. 331–344, 2001.
6. P.-Y. Yan, "Understanding bossung curve asymmetry and focus shift effect in euv lithography," *Proc. of SPIE* **4562**, pp. 1–9, 2001.
7. M. Lam, K. Adam, and A. Neureuther, "Domain decomposition methods for simulation of printing and inspection of phase defects," *Proceedings of the SPIE* **5040**, pp. 1492–1501, 2003.
8. J. Tirapu-Azpiroz, P. Burchard, and E. Yablonovitch, "Boundary layer model to account for thick mask effects in photolithography," *Proceedings of the SPIE* **5040**, pp. 1611–1619, 2003.
9. H. J. Levinson, *Principles of Lithography*, SPIE Press, 2001.
10. K. Adam, Y. Granik, A. Torres, and N. Cobb, "Improved modeling performance with an adapted vectorial formulation of the hopkins imaging equation," *Proceedings of the SPIE* **5040**, pp. 78–90, 2003.
11. J. Tirapu-Azpiroz and E. Yablonovitch, "Modeling of near-field effects in sub-wavelength deep ultraviolet lithography," To appear in *Future Trends of Microelectronics 2003*, S. Luryi, J. Xu, and A. Zaslavsky, eds., Wiley Interscience.
12. E. Wolf and Y. Li, "Conditions for the validity of the debye integral representation of focused fields," *Optics Communications* **39, No 4**, pp. 205–210, 1981.
13. D. G. Flagello, T. Milster, and A. E. Rosenbluth, "Theory of high-na imaging in homogeneous thin films," *J. Opt. Soc. Am. A* **13, No 1**, pp. 53–64, 1996.
14. A. K. Wong and A. R. Neureuther, "Rigorous three-dimensional time-domain finite-difference electromagnetic simulation for photolithographic applications," *IEEE Trans. on Semiconductor Manufacturing* **8, No 4**, pp. 419–431, Nov. 1995.